J. Zhang, J.D. Biggs, D. Ye, Z. Sun
Finite-Time Attitude Set-Point Tracking for Thrust-Vectoring Spacecraft Rendezvous
Aerospace Science and Technology, Vol. 96, 2020, 105588 (10 pages)
doi:10.1016/j.ast.2019.105588

Finite-time attitude set-point tracking for thrust-vectoring spacecraft rendezvous

Jianqiao Zhang[a,*], James D. Biggs[b], Dong Ye[a], Zhaowei Sun[a]

[a]*Research Center of Satellite Technology, Harbin Institute of Technology, Harbin, 150001, P.R. China.*
[b]*Department of Aerospace Science and Technology, Politecnico di Milano, Milan, 20156, Italy.*

Abstract

This paper addresses the optimal orbit rendezvous problem for thrust-vectoring spacecraft. In this scenario, the chaser spacecraft is equipped with only one impulsive thruster fixed in the body frame, while the thrust direction is pointed using attitude control of the spacecraft. An improved particle swarm optimization (PSO) algorithm is employed to generate an optimal multiple-burn rendezvous trajectory in terms of thruster pulse duration and required attitude. A coordinate-free, finite-time, attitude control is developed to ensure that this required thrust vector is met exactly at the prescribed time. The proposed orbit-attitude guidance algorithm is compared with one which utilizes a conventional PSO and is shown to significantly improve performance. In addition, the set-point attitude control is illustrated, in simulation, to deliver the required thrust direction at the prescribed time.

Keywords: Orbit rendezvous; Thrust-vectoring spacecraft; Particle swarm optimization; Coordinate-free; Finite-time attitude control.

1. Introduction

Autonomous rendezvous and proximity operations (RPOs) are key enabling technologies for many anticipated space missions such as removing space debris, repairing failed spacecraft on orbit, refueling, and for operations with the International Space Station [1–8]. In order for such missions to be realized, guidance and control algorithms must meet strict requirements on precision, while they should be optimal, robust and computationally efficient [9]. RPO can be divided into three phases: far-field rendezvous, near-field rendezvous, and final approach. Progress has been made in this direction for different RPO phases, such as optimal orbit trajectory generation for far and near field rendezvous [1], integrated guidance and control for near field rendezvous [3, 4], and robust relative position and attitude control for the final approach [5, 6]. In general, the guidance and control for RPO assume that control forces can be provided instantaneously

*Corresponding author
Email addresses: zhangjianqiao@hit.edu.cn (Jianqiao Zhang), jamesdouglas.biggs@polimi.it (James D. Biggs), yed@hit.edu.cn (Dong Ye), sunzhaowei@hit.edu.cn (Zhaowei Sun)

in any direction. However, for many future rendezvous and docking missions the spacecraft will be thrust-vectored. Moreover, the spacecraft will have the ability to control a single force vector fixed in the body axis, which can be pointed by using attitude control [10]. Thrust-vectoring spacecraft can allow reduced mass and volume savings and are therefore particularly suitable for the next generation of micro and nano spacecraft [11]. Furthermore, using a single thruster for RPOs significantly reduces the risk of damaging the target with thruster plumes on approach.

This paper is focused on the trajectory tracking problem for far and near-field rendezvous, where the chaser spacecraft is equipped with a single impulsive thruster and reaction wheels for attitude control. The target and chaser spacecraft are initialized on two non-coplanar, non-circular orbits, and the chaser spacecraft is then required to track the position and velocity of the target in a fixed time, while minimizing fuel consumption. This problem can be formulated in two parts (i) the generation of an optimal reference rendezvous to yield a required time and $\Delta \boldsymbol{v}$. Specifically, for a thrust-vectoring spacecraft, this trajectory is converted into a required attitude and thruster pulse duration at a prescribed time and (ii) an attitude set-point tracking problem that must match the pointing direction precisely at the prescribed time.

The initial stage requires the generation of attitude set-points and thruster pulse durations which is achieved using a combination of particle swarm optimization (PSO) and the Lambert method. It is possible to generate the initial optimal trajectory using a plethora of methods that already exist in the literature, such as numerical shooting [12], transcription methods [13], and heuristic methods such as genetic algorithms (GA) [14], ant colony optimization [15], and particle swarm optimization (PSO) [16]. PSO is favored in this paper due to its fast convergence, simplicity of implementation, and lower computational complexity compared with other heuristics methods [17, 18]. Usually the lack of dynamic regulation in PSO can lead to convergence to local optima, known as the premature phenomenon [19]. However, adapting the PSO parameters iteratively enables the algorithm to avoid this premature phenomenon. The approach here extends [1] by adapting a constrained PSO to the guidance of rendezvous spacecraft operating in general (non-coplanar, non-circular) orbits. Specifically, the PSO is used to generate a four stage maneuver each requiring a specific thruster pulse duration and required attitude at a specified time. Thus, for this approach to be viable, the required attitude must also guarantee that the prescribed thruster direction is precisely met in a specific finite time.

The required reference attitude is computed by the required vector of $\Delta \boldsymbol{v}$, and is defined naturally on the Special Orthogonal Group SO(3), whereby the required thrust direction corresponds to a column vector of the desired attitude matrix. However, it is difficult to construct a control scheme on SO(3) directly. Thus, by introducing a smooth positive-definite configuration error function to measure the attitude tracking error, a co-ordinate free, finite-time, attitude control is proposed here to guarantee that the set-point attitudes along the desired rendezvous are met. Formulating the attitude guidance in this co-ordinate free way allows the control to be developed using a natural rotation error metric [20], while avoiding singularities associated

with Modified Rodrigues Parameters (MRPs) such as in [21, 22], and avoiding problems with ambiguous global representations associated with unit quaternions such as in [23–25]. Moreover, unit quaternions are often used for their computational efficiency, but are ambiguous since the mapping between quaternions and a physical rotation is not unique. This can lead to problems of un-winding whereby two different quaternions corresponding to the same physical orientation can have opposing stability properties i.e. one can be stable while the other unstable. Thus, the un-winding problem refers to the situation where a control induces a winding rotation away from the unstable desired quaternion to the corresponding stable quaternion. Finite-time attitude control has been developed before on SO(3) [26–30]. However, we advance the state-of-the-art here by developing a co-ordinate-free fast terminal sliding mode controller (FTSMC). This proposed finite-time controller does not require the computation of the second order derivative of the error function that is necessary to guarantee finite-time stability in [29, 30]. This feature means that it is more computationally efficient to implement, while it maintains a guaranteed finite-time convergence.

The remainder of this paper is organized as follows: In Section 2, the mathematical model of the RPO is developed, and the control objective of this paper is presented. An improved PSO algorithm is proposed in Section 3 to generate the optimal trajectory of the RPO. In Section 4, a finite-time attitude control scheme is designed to track the directions of the optimal impulse vectors, along with the proof of the stability of the closed-loop attitude system. In Section 5, two cases of numerical simulations are conducted to illustrate the effectiveness of the PSO and the finite-time attitude controller.

2. Problem formulation

The six-degree-of-freedom (6-DOF) dynamics of the thrust-vectoring chaser spacecraft are defined in this section and the three reference frames used are depicted in Fig 1.

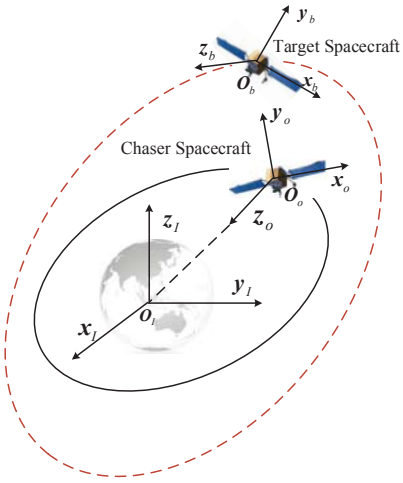

Fig. 1. Illustration of the coordinate frames.

(a) The standard Earth centered inertial frame $\mathscr{F}_I(x_I, y_I, z_I)$ is located at the Earth's mass center, x_I points to the Earth's vernal equinox, z_I is along the Earth's rotation axis, and y_I is obtained by the right-hand rule. Superscript I is used to represent a vector in this frame.

(b) The orbital coordinate frame $\mathscr{F}_o(x_o, y_o, z_o)$ is a right-handed orthogonal system and located at the spacecraft's mass center, z_o is along the opposite direction of the spacecraft's position vector in $\mathscr{F}_I$, y_o points to the direction of angular momentum, and x_o completes the right-handed orthonormal frame.

(c) The body-fixed frame $\mathscr{F}_b(x_b, y_b, z_b)$, whose origin is the mass center of the spacecraft and its three axes are parallel to its principal body axes. Superscript b denotes the frame of reference of the vector.

2.1. 6-DOF dynamics of the chaser spacecraft

The chaser spacecraft studied in this paper is thrust-vectored with one impulsive thruster fixed in its z_b axis. Thus, this system is highly coupled with the attitude of the spacecraft and the 6-DOF dynamics must be used:

$$\begin{cases} \dot{\boldsymbol{r}} = \boldsymbol{v} \\ \dot{\boldsymbol{v}} = -\dfrac{\mu}{\|\boldsymbol{r}\|^3}\boldsymbol{r} + \dfrac{1}{m}\boldsymbol{R}\boldsymbol{F} \\ \dot{\boldsymbol{R}} = \boldsymbol{R}\boldsymbol{\Omega}^{\times} \\ \dot{\boldsymbol{\Omega}} = \boldsymbol{J}^{-1}(-\boldsymbol{\Omega}^{\times}\boldsymbol{J}\boldsymbol{\Omega} + \boldsymbol{U}) \end{cases} \tag{1}$$

where $\boldsymbol{r} \in \mathbb{R}^{3\times1}$ and $\boldsymbol{v} \in \mathbb{R}^{3\times1}$ are the spacecraft's position and translational velocity in $\mathscr{F}_I$ respectively, $\mu = 398600.47\text{km}^3/s^2$ is the Earth's gravitational constant, $\| \boldsymbol{r} \|$ is the Euclidean norm of $\boldsymbol{r}$, m is the mass of the spacecraft, $\boldsymbol{F} = [0\ 0\ F]^{\mathrm{T}} \in \mathbb{R}^{3\times1}$ is the force generated by the unilateral impulsive thruster along z_b axis, $\boldsymbol{R} \in \mathrm{SO}(3)$ is the rotation matrix from $\mathscr{F}_b$ to $\mathscr{F}_I$, $\mathrm{SO}(3) = \{\boldsymbol{R} \in \mathbb{R}^{3\times3} : \boldsymbol{R}^{\mathrm{T}}\boldsymbol{R} = \boldsymbol{I}_{3\times3}, \det(\boldsymbol{R}) = 1\}$ is a Lie group, $\boldsymbol{\Omega} \in \mathbb{R}^{3\times1}$ is the angular velocity expressed in $\mathscr{F}_b$, $(\boldsymbol{\Omega})^{\times}$ is the skew-symmetric matrix of $\boldsymbol{\Omega}$, $\boldsymbol{U}$ is the torque applied on the spacecraft generated by reaction wheels, and $\boldsymbol{J}$ is the inertia matrix of the spacecraft.

2.1.1. Orbit dynamics for spacecraft with impulsive thruster

Assuming that the orbit rendezvous for a chaser spacecraft with a non-coplanar target spacecraft in a fixed time can be realized by N impulses, and $\Delta\boldsymbol{v}_i, (i = 1, \cdots, N)$ is the velocity change at each step, then

the relationships of the positions and velocities before and after an impulse can be obtained

$$\begin{cases} t_i^+ = t_i^- \\ \boldsymbol{r}_i^+ = \boldsymbol{r}_i^- \\ \boldsymbol{v}_i^+ = \boldsymbol{v}_i^- + \Delta\boldsymbol{v}_i \end{cases} \tag{2}$$

where $(\cdot)^-$ and $(\cdot)^+$ mean the parameters before and after an impulse, respectively.

For the spacecraft rendezvous problem, it is assumed that the trajectory of the chaser spacecraft after one impulse is Keplerian orbit with elliptic type [1]. Then the corresponding semimajor axis a_i, eccentricity e_i, inclination I_i, mean anomaly M_i, argument of perigee ω_i, and right ascension of ascending node W_i after ith impulse can be obtained once $\boldsymbol{r}_i^+$ and $\boldsymbol{v}_i^+$ are known. Moreover, during the ith impulse and $(i+1)$th impulse, the position and velocity of the chaser spacecraft can be calculated by the orbit elements [31]. These relationships can be expressed by

$$\begin{cases} \big(a_i, e_i, I_i, M_i, \omega_i, W_i\big) = f_1\big(\boldsymbol{r}_i, (\boldsymbol{v}_i^- + \Delta\boldsymbol{v}_i)\big) \\ \big(\boldsymbol{r}(t_i + \Delta t^i), \boldsymbol{v}(t_i + \Delta t^i)\big) = f_2\big(a_i, e_i, I_i, M_i, \omega_i, W_i, \Delta t^i\big) \end{cases} \tag{3}$$

where $\Delta t^i \in [t_i, t_{i+1}]$, and the initial orbit elements of the chaser spacecraft is $\big(a_0, e_0, I_0, M_0, \omega_0, W_0\big) = \boldsymbol{f}_1\big(\boldsymbol{r}_1, \boldsymbol{v}_1^-\big)$. Since for the eccentric anomaly E, we have

$$E = M + e \cdot \sin(E) \tag{4}$$

Thus $E(t_i^+)$ and $E(t_{i+1}^-)$ can be obtained by M_i, M_{i+1}^- and e_i iteratively. Then, we have $E(t_{i+1}^-) = E(t_i^+) + \Delta E_i$, which can be used to calculate the running time of ith impulse through Kepler's law

$$\Delta t_i = t_{i+1} - t_i = f_3(\Delta E_i) = \sqrt{\frac{a_i^3}{\mu}}\Big\{\Delta E_i - e_i\big\{\sin\big(E(t_{i+1}^-)\big) - \sin\big(E(t_i^+)\big)\big\}\Big\} \tag{5}$$

2.1.2. Relative rotational dynamics of the chaser spacecraft

The desired $\Delta\boldsymbol{v}_i$ is generated by the orbital guidance approach and its direction vecotr is aligned with the desired thrust direction fixed in the body frame $\boldsymbol{z}_{bi}^I = \Delta\boldsymbol{v}_i / \parallel \Delta\boldsymbol{v}_i \parallel$. Taking $\boldsymbol{z}_{bi}^I$ as input, this subsection is in charge of computing a reference attitude and angular velocity that are feasible in the following sense [10]: $\dot{\boldsymbol{R}}_{di} = \boldsymbol{R}_{di}\boldsymbol{\Omega}_{di}^{\times}(t),\ \forall t \geq 0,\ \boldsymbol{\Omega}_{di} \in C^1 \cap L_\infty$, and then developing the relative rotational dynamics of the system. The procedure to define $\boldsymbol{R}_{di}$ is described below:

(a) Select an appropriate vector $\boldsymbol{s}_d \in \boldsymbol{C}^2(\mathbb{R}^3)$, which is transverse to $\boldsymbol{z}_{bi}^I$. $\boldsymbol{s}_d$ can be selected depending on the mission requirements. For example, it can be equated to the velocity vector of the spacecraft or

the Sun direction. An arbitrary choice is made here since no specific mission requirements are specified as in [27]. We let $\boldsymbol{z}_{bi}^I = [z_1\ z_2\ z_3]^{\mathrm{T}} \in \mathbb{S}^2 \subset \mathbb{R}^3$, then

$$\boldsymbol{s}_d = \begin{bmatrix} z_2 + z_3 \\ z_3 - z_1 \\ -z_1 - z_2 \end{bmatrix} \tag{6}$$

which is orthogonal to $\boldsymbol{z}_{bi}^I$.

(b) Compute $\boldsymbol{y}_{bi}^I$ by $\boldsymbol{y}_{bi}^I = \dfrac{\boldsymbol{z}_{bi}^I \times \boldsymbol{s}_d}{\parallel \boldsymbol{z}_{bi}^I \times \boldsymbol{s}_d \parallel} = \boldsymbol{R}_{di} y_b$.

(c) Compute $\boldsymbol{x}_{bi}^I$ by $\boldsymbol{x}_{bi}^I = \boldsymbol{y}_{bi}^I \times \boldsymbol{z}_{bi}^I = \boldsymbol{R}_{di} x_b$. The desired attitude of the ith impulse is then defined as $\boldsymbol{R}_{di} = [\boldsymbol{x}_{bi}^I\ \boldsymbol{y}_{bi}^I\ \boldsymbol{z}_{bi}^I] \in \mathrm{SO}(3)$.

A smooth positive-definite configuration error function $\Psi : \mathrm{SO}(3) \times \mathrm{SO}(3) \to \mathbb{R}$ is usually adopted to measure the error between the actual and desired attitude [28, 29], and attitude controller is designed based on the error function. In this paper, the so-called modified trace function defined on SO(3) in [32] is utilized to describe the attitude error

$$\Psi_i(\boldsymbol{R}_i, \boldsymbol{R}_{di}) = \frac{1}{2}\mathrm{tr}\big[\boldsymbol{K}(\boldsymbol{I}_3 - \boldsymbol{R}_{di}^{\mathrm{T}}\boldsymbol{R}_i)\big] \tag{7}$$

where $\boldsymbol{K} = \mathrm{diag}(k_1\ k_2\ k_3) > 0$. Taking the derivative of Ψ_i, we can get the attitude error $\boldsymbol{e}_{\boldsymbol{R}i} : \mathrm{SO}(3) \times \mathrm{SO}(3) \to \mathbb{R}^3$ and the angular velocity tracking error $\boldsymbol{e}_{\Omega i} : \mathrm{SO}(3) \times \mathbb{R}^3 \times \mathrm{SO}(3) \times \mathbb{R}^3 \to \mathbb{R}^3$

$$\frac{\mathrm{d}}{\mathrm{dt}}(\Psi_i(\boldsymbol{R}_i, \boldsymbol{R}_{di})) = \boldsymbol{e}_{\boldsymbol{R}i} \cdot \boldsymbol{e}_{\boldsymbol{\Omega}i} \tag{8}$$

$$\boldsymbol{e}_{\boldsymbol{R}i} = \frac{1}{2}(\boldsymbol{K}\boldsymbol{R}_{di}^{\mathrm{T}}\boldsymbol{R}_i - \boldsymbol{R}_i^{\mathrm{T}}\boldsymbol{R}_{di}\boldsymbol{K})^{\vee} \tag{9}$$

$$\boldsymbol{e}_{\boldsymbol{\Omega}i} = \boldsymbol{\Omega}_i - \boldsymbol{R}_i^{\mathrm{T}}\boldsymbol{R}_{di}\boldsymbol{\Omega}_{di} \tag{10}$$

where $(\cdot)^{\vee} : \varsigma o(3) \to \mathbb{R}^3$ is the inverse mapping of $(\cdot)^{\times}$. Taking the derivative of $\boldsymbol{e}_{\boldsymbol{R}i}$ and $\boldsymbol{e}_{\boldsymbol{\Omega}i}$, and substituting Eq.(1) into the results, we can get the relative attitude dynamics

$$\dot{\boldsymbol{e}}_{\boldsymbol{R}i} = \boldsymbol{G}_i(\boldsymbol{R}_i, \boldsymbol{R}_{di})\boldsymbol{e}_{\boldsymbol{\Omega}i} \tag{11}$$

$$\dot{\boldsymbol{e}}_{\boldsymbol{\Omega}i} = \boldsymbol{J}^{-1}(-\boldsymbol{\Omega}_i^{\times}\boldsymbol{J}\boldsymbol{\Omega}_i + \boldsymbol{U}_i) + \boldsymbol{\Omega}_i^{\times}\boldsymbol{R}_{ei}^{\mathrm{T}}\boldsymbol{\Omega}_{di} - \boldsymbol{R}_{ei}^{\mathrm{T}}\dot{\boldsymbol{\Omega}}_{di} \tag{12}$$

where $\boldsymbol{G}_i(\boldsymbol{R}_i, \boldsymbol{R}_{di}) = \frac{1}{2}(\mathrm{tr}(\boldsymbol{R}_{ei}^{\mathrm{T}}\boldsymbol{K})\boldsymbol{I}_3 - \boldsymbol{R}_{ei}^{\mathrm{T}}\boldsymbol{K})$. The property of the relative attitude dynamics is [33]

Property 1. *$\Psi(\boldsymbol{R}, \boldsymbol{R}_d)$ is locally quadratic, and satisfies*

$$b_1 \parallel \boldsymbol{e}_{\boldsymbol{R}}(\boldsymbol{R}, \boldsymbol{R}_d) \parallel^2 \leq \Psi(\boldsymbol{R}, \boldsymbol{R}_d) \leq b_2 \parallel \boldsymbol{e}_{\boldsymbol{R}}(\boldsymbol{R}, \boldsymbol{R}_d) \parallel^2 \tag{13}$$

where $b_1 = (h_1/h_2 + h_3)$, $b_2 = (h_1 h_4/h_5(h_1 - \psi))$, $h_1 = \min\{k_1 + k_2, k_2 + k_3, k_3 + k_1\}$, $h_2 = \max\{(k_1 - k_2)^2, (k_2 - k_3)^2, (k_3 - k_1)^2\}$, $h_3 = \max\{(k_1 + k_2)^2, (k_2 + k_3)^2, (k_3 + k_1)^2\}$, $h_4 = \max\{k_1 + k_2, k_2 + k_3, k_3 + k_1\}$, $h_5 = \min\{(k_1 + k_2)^2, (k_2 + k_3)^2, (k_3 + k_1)^2\}$, and ψ is a positive constant and satisfies $\Psi(\boldsymbol{R}, \boldsymbol{R}_d) < \psi < h_1$.

2.2. Constraint modeling and handling

The constraints during the trajectory tracking process are assumed to be the boundary conditions and the actuator constraints of the chaser spacecraft.

2.2.1. Matching the boundary conditions

The rendezvous problem consists of determining the optimal positions $\boldsymbol{r}_i$, the directions and magnitudes of $\Delta\boldsymbol{v}_i$ such that the trajectory of the target spacecraft can be tracked in the predefined time t_f. At the terminal time t_f, both the positions and velocities of the two spacecraft must be equal to each other, which means the following terminal conditions must be satisfied

$$\begin{cases} \boldsymbol{r}_{\mathrm{target}}(t_f) = \boldsymbol{r}_N^+(t_f) = \boldsymbol{r}_N^-(t_f) \\ \boldsymbol{v}_{\mathrm{target}}(t_f) = \boldsymbol{v}_N^+(t_f) = \boldsymbol{v}_N^-(t_f) + \Delta\boldsymbol{v}_N \\ t_f = t_N - t_1 = \Delta t_1 + \cdots + \Delta t_{N-1} \end{cases} \tag{14}$$

To meet the above boundary conditions, the last two velocity impulses will be computed via the Lambert theorem. The trajectory generated by the $N-2$ ($N \geq 2$) impulses can be obtained through Eq. (3), and also the running time $\Delta t_1 + \cdots + \Delta t_{N-2} \geq 0$ by Eq. (5). Thus, the initial position $\boldsymbol{r}_{N-1}$, the final position $\boldsymbol{r}_{tf}$, and the running time Δt_{N-1} are all known. Then, we can obtain the relationship between the transfer time Δt_{N-1} and the semimajor axis a_{N-1} from Lagrange's formulation of the Lambert problem, which can be expressed as

$$\Delta t_{N-1} = \sqrt{\frac{a_{N-1}^3}{\mu}}\left[2n\pi + (\delta_1 - \delta_2) - (\sin\delta_1 - \sin\delta_2)\right] \tag{15}$$

where n is the number of revolutions, $\cos\delta_1 = 1 - s/a_{N-1}$, $\cos\delta_2 = \cos\delta_1 + d/a_{N-1}$, $d = \parallel \boldsymbol{r}_{N-1} - \boldsymbol{r}_{tf} \parallel$, $s = (\parallel \boldsymbol{r}_{N-1} \parallel + \parallel \boldsymbol{r}_{tf} \parallel + d)/2$. It should be noted that multiple-revolution solutions are not considered for

the $(N-1)$th Keplerian arc, which means that $n=0$. When $a_{N-1}=s/2$, the transfer orbit is minimum-energy, and when $a_{N-1}>s/2$, there are two solutions, namely the short-path orbit and the long-path orbit. Once Δt_{N-1} and a_{N-1} have been obtained, the semilatus rectum of the Lambert orbit is [34]

$$p=\sin\Big(\frac{\delta_1+\delta_2}{2}\Big)\frac{\parallel \boldsymbol{r}_{N-1}\parallel\parallel \boldsymbol{r}_{tf}\parallel -\boldsymbol{r}_{N-1}^{\mathrm{T}}\boldsymbol{r}_{tf}}{d\cdot\sin\Big(\frac{\delta_1-\delta_2}{2}\Big)} \tag{16}$$

Then, the velocities of the Lambert orbit at $\boldsymbol{r}_{N-1}$ and $\boldsymbol{r}_{tf}$ are [34]

$$\begin{aligned}\boldsymbol{v}_{N-1}^{+}&=\frac{\sqrt{\mu p}}{\parallel \boldsymbol{r}_{N-1}\parallel\parallel \boldsymbol{r}_{tf}\parallel\sin\theta}\Big[\Big(\frac{\parallel \boldsymbol{r}_{tf}\parallel}{p}(1-\cos\theta)-1\Big)\boldsymbol{r}_{N-1}+\boldsymbol{r}_{tf}\Big]\\ \boldsymbol{v}_{N}^{-}&=\frac{\sqrt{\mu p}}{\parallel \boldsymbol{r}_{N-1}\parallel\parallel \boldsymbol{r}_{tf}\parallel\sin\theta}\Big[\Big(1-\frac{\parallel \boldsymbol{r}_{N-1}\parallel}{p}(1-\cos\theta)\Big)\boldsymbol{r}_{tf}-\boldsymbol{r}_{N-1}\Big]\end{aligned} \tag{17}$$

where $\theta=\arccos\big(\frac{\boldsymbol{r}_{N-1}^{\mathrm{T}}\boldsymbol{r}_{tf}}{\|\boldsymbol{r}_{N-1}\|\|\boldsymbol{r}_{tf}\|}\big)$ is the transfer angle between the two position vectors. Then the last two impulsive velocity changes can be obtained $\Delta\boldsymbol{v}_{N-1}=\boldsymbol{v}_{N-1}^{+}-\boldsymbol{v}_{N-1}^{-}$, and $\Delta\boldsymbol{v}_{N}=\boldsymbol{v}_{\mathrm{target}}(t_f)-\boldsymbol{v}_{N}^{-}$. Moreover, $a_i>0$ should be guaranteed such that the assumption of the rendezvous trajectory composed by $N-1$ Keplerian arcs holds. In addition, from Eq. (5) we can see that the running time of the rendezvous process can be expressed by a function of eccentric anomaly ΔE_i. Thus, $\Delta E_i\geq 0$ and $t_f=f_3(\Delta E_1)+\cdots+f_3(\Delta E_{N-1})$ must hold. Thereby, the boundary conditions are all satisfied.

2.2.2. Control limits

Since the configuration of attitude actuators is fully-actuated with reaction wheels, thus only the upper bound of $\boldsymbol{U}$ needs to be considered. The constraint function can be expressed as [35]

$$\boldsymbol{U}_j=\mathrm{sign}(\boldsymbol{U}_j)\min\big(|\boldsymbol{U}_j|,\ u_{\max}\big), j=1,2,3 \tag{18}$$

where $u_{\max}$ is the maximum torque that the actuators can provide along the spacecraft body axes.

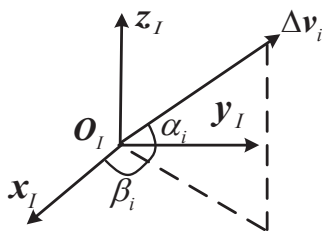

Fig. 2. The decomposition of $\Delta\boldsymbol{v}_i$.

In the case of impulsive thruster, our focus is on the magnitude and direction of the impulsive velocity

change $\Delta \boldsymbol{v}_i$, which can be decomposed as shown in Fig. 2. Then, $\Delta \boldsymbol{v}_i$ can be represented by

$$\Delta \boldsymbol{v}_i = \begin{bmatrix} \Delta v_i \cdot \cos\alpha_i \cdot \cos\beta_i \\ \Delta v_i \cdot \cos\alpha_i \cdot \sin\beta_i \\ \Delta v_i \cdot \sin\alpha_i \end{bmatrix} \tag{19}$$

where $\Delta v_i = \| \Delta \boldsymbol{v}_i \|$. Thus, the limitations on the thruster can be obtained by restricting $0 \leq \Delta v_i \leq \Delta v_{\max}$, $-\pi/2 \leq \alpha_i \leq \pi/2$, and $0 \leq \beta_i \leq 2\pi$. $\Delta v_{\max}$ is the upper bound of the velocity search space.

2.3. Control objective

The cost function that needs to be optimized is

$$\min J = \sum_{i=1}^{N} \Delta v_i \tag{20}$$

while the constraints and boundary conditions in Eqs. (14) and (19) must be satisfied. As illustrated in [36], as many as four impulses are enough for an optimal fixed-time rendezvous problem. Thus, in this paper we set $N = 4$. In addition, an attitude controller is required such that the optimized thruster vector $\Delta \boldsymbol{v}_i$ can be tracked by the chaser spacecraft in finite-time to guarantee the thruster could fire in time.

3. Optimal rendezvous trajectory generation via PSO

PSO was first introduced by Kennedy and Eberhart [37] by mimicking the unpredictable behavior of bird flock while searching for food and sharing information among the flock. Conventional PSO is unable to deal with equality and inequality constraints placed on the unknown parameters to be optimized [1]. Thus, many improved PSO (IPSO) methods, which are able to deal with constraints, have been proposed and applied to solve spacecraft trajectory optimization problems, such as optimal spacecraft rendezvous [1], optimal orbit transfer [19], and spacecraft optimal reentry [18, 38]. Based on conventional PSO, an improved PSO is proposed in this section to develop the optimal RPO trajectory.

3.1. Conventional PSO

The PSO technique is a population-based method with N_1 particles. Each particle $k(k = 1 \cdots N_1)$ is associated with a position $\boldsymbol{X}_k = (x_{k,1}, x_{k,2}, \cdots, x_{k,D})$ and a velocity $\boldsymbol{\nu}_k = (\nu_{k,1}, \nu_{k,2}, \cdots, \nu_{k,D})$, where D is the dimension of the search space (in this study $D = 8$, $\boldsymbol{X} = \{\Delta v_1, \alpha_1, \beta_1, \Delta E_1, \Delta v_2, \alpha_2, \beta_2, \Delta E_2\}$), $\boldsymbol{X}_k$, corresponding to a value of the objective function, represents a possible solution to the optimization problem, and $\boldsymbol{\nu}_k$ is used to update $\boldsymbol{X}_k$. The final optimal solution is sought by moving the particles in the search space with $\boldsymbol{\nu}_k$. If $\boldsymbol{P}_k = (p_{k,1}, p_{k,2}, \cdots, p_{k,D})$ is the best position of the kth particle so far, and

$\boldsymbol{P}_g = (p_{g,1}, p_{g,2}, \cdots, p_{g,D})$ is the best position of the entire swarm in the current iteration, then the position of the kth particle can be updated by [38]

$$\begin{cases} \nu_{k,d}^{t+1} = \varpi \nu_{k,d}^{t} + c_1 \mathrm{rand}_1(\cdot)(p_{k,d} - x_{k,d}^{t}) + c_2 \mathrm{rand}_2(\cdot)(p_{g,d} - x_{k,d}^{t}) \\ x_{k,d}^{t+1} = x_{k,d}^{t} + \nu_{k,d}^{t+1} \end{cases} \tag{21}$$

where $d = 1, \cdots, D$, t is the current iteration number, $\mathrm{rand}_1(\cdot)$ and $\mathrm{rand}_2(\cdot)$ are random numbers uniformly distributed in the interval $[0, 1]$, and ϖ is the inertia weight. Initially, ϖ is set to a static value. Then, research conducted by Shi and Eberhart showed that a linearly decreasing ϖ will improve the PSO performance better [39]. $c_1 > 0$ is the cognitive component, which reflects the importance of the personal best position on the update of the particle, $c_2 > 0$ is the social component, which reflects how much confidence the particle has in the swarm, and these two parameters are commonly set to 2.

3.2. The improved PSO of this paper

For a constrained optimization problem, usually the constraints can be expressed by equalities and inequalities, then the nonlinear programming problem can be expressed mathematically by

$$\begin{cases} \min J = f(\boldsymbol{X}), \boldsymbol{X} = [x_1, \cdots x_D] \\ \text{s.t.} \\ g_\ell(\boldsymbol{X}) \geq 0, \ell = 1, 2, \cdots, q_1 \\ h_\hbar(\boldsymbol{X}) = 0, \hbar = q_1 + 1, q_1 + 2, \cdots, q_1 + q_2 \end{cases} \tag{22}$$

where $\boldsymbol{X}$ is a vector composed by the control variables of the optimization problem, and q_1 and q_2 are the numbers of inequality constraints and equality constraints, respectively.

Since the equality constraints will reduce the degrees of freedom of the optimization problem and the inequality constraints only reduce the search space of the possible solutions, it is common to transfer equality constraints into inequality constraints with

$$g_{q_1+\hbar}(\boldsymbol{X}) = h_\hbar(\boldsymbol{X}) + \varepsilon \geq 0 \tag{23}$$

where $\varepsilon > 0$ is the threshold. Then, the constraints considered are only the inequality terms $g_\ell(\boldsymbol{X}) \geq 0, \ell = 1, 2, \cdots, (q_1 + q_2)$. To address the constrained optimization problem described by Eq. (22), a penalty function is constructed using the multiplier method [40] to incorporate constraints,

$$\Phi(\boldsymbol{X}, \zeta, \sigma) = f(\boldsymbol{X}) + \frac{1}{2\sigma} \sum_{\ell=1}^{q_1+q_2} \left\{ \max^2\big(0, \zeta_\ell - \sigma g_\ell(\boldsymbol{X})\big) - \zeta_\ell^2 \right\} \tag{24a}$$

$$\zeta_\ell(t+1) = \max\Big(0, \zeta_\ell(t) - \sigma g_\ell\big(\boldsymbol{X}(t)\big)\Big) \tag{24b}$$

where ζ is the multiplier, and $\sigma > 0$ is a sufficient large scalar.

In practice, the unknown parameters $x_{k,d}$ are constrained within suitable ranges, and are described by

$$x_{l,d} \leq x_{k,d} \leq x_{u,d} \tag{25}$$

where $x_{l,d}$ is the lower bound and $x_{u,d}$ is the upper bound of $x_{k,d}$, respectively. Consequently, the corresponding velocity should also be constrained by

$$\nu_{l,d} \leq \nu_{k,d} \leq \nu_{u,d} \tag{26}$$

where the lower bound is $\nu_{l,d} = x_{l,d} - x_{u,d}$ and the upper bound is $\nu_{u,d} = x_{u,d} - x_{l,d}$. These bounds are designed due to the fact that if $\nu_{k,d} > x_{u,d}$ or $\nu_{k,d} < x_{l,d}$, no matter where $x_{k,d}(t)$ starts from, $x_{k,d}(t+1)$ would violate the limitations in Eq. (25). If $x_{k,d}$ is out of the interval of Eq. (25), it will be changed to [38]

$$x_{k,d}^t = \begin{cases} \bar{x}_d^t + \text{rand}(\cdot)(x_{l,d} - \bar{x}_d^t), & if \quad x_{k,d}^t < x_{l,d} \\ \bar{x}_d^t + \text{rand}(\cdot)(x_{u,d} - \bar{x}_d^t), & if \quad x_{k,d}^t > x_{u,d} \end{cases} \tag{27}$$

where $\bar{x}_d^t = \sum_{k=1}^{N_1} x_{k,d}^t / N_1$ represents the mid-value of the swarm on the dimension d. If $\nu_{k,d}$ is out of the limitations in Eq. (26), it will be assigned to

$$\nu_{k,d}^t = \begin{cases} \nu_{l,d}, & if \quad \nu_{k,d}^t < \nu_{l,d} \\ \nu_{u,d}, & if \quad \nu_{k,d}^t > \nu_{u,d} \end{cases} \tag{28}$$

It can be found that the function in (24a) does not require σ to be infinite, and when σ is large enough, $\Phi(\boldsymbol{X}, \zeta, \sigma)$ can be minimized to get the minimum value of $f(\boldsymbol{X})$. In [1], the information of the position and velocity of an infeasible particle is not used for velocity update. In contrast to [1], here the information of an infeasible particle is used, and as shown in [18], the information of the infeasible particle with a best fitness function value can improve the convergence of the optimizer. In addition, for the improvement of the global search ability and the performance of the PSO, a linearly decreasing ϖ in [39] is utilized

$$\varpi = (\varpi_0 - \varpi_f)\frac{t_{\max} - t}{t_{\max}} + \varpi_f \tag{29}$$

where $t_{\max}$ is the maximum iteration number, and ϖ_0 and ϖ_f are the initial and final values of ϖ, respectively. Initially, a larger ϖ_0 means that all particles can have a very large speed, which can help the global

searching. At the end, a smaller ϖ_f means the particles can search more efficiently near to the optimal point such that the convergence of the algorithm is guaranteed. Furthermore, as illustrated in [41], particles with smaller self-learning ability and larger social learning ability will speed up the swarm to converge to its optimal position, and particles with larger self-learning ability and smaller social learning ability will guarantee the swarm has a strong global searching, which means that if c_1 decreases with time and c_2 increases with time, then these dynamical changes will have the similar effect as the change of ϖ on the particles. Therefore, we design c_1 and c_2 as follows

$$\begin{cases} c_1 = \gamma_1 - \Theta_1 \dfrac{t}{t_{\max}} \\ c_2 = \gamma_2 + \Theta_2 \dfrac{t}{t_{\max}} \end{cases} \tag{30}$$

where $\gamma_1, \gamma_2, \Theta_1, \Theta_2$ are all positive constants.

3.3. Thruster attitudes and pulse durations generated by IPSO

The flowchart of applying the improved PSO developed in this paper to generate the required thruster attitude and its pulse duration of each step is shown in Fig. 3, which can be concluded as follows

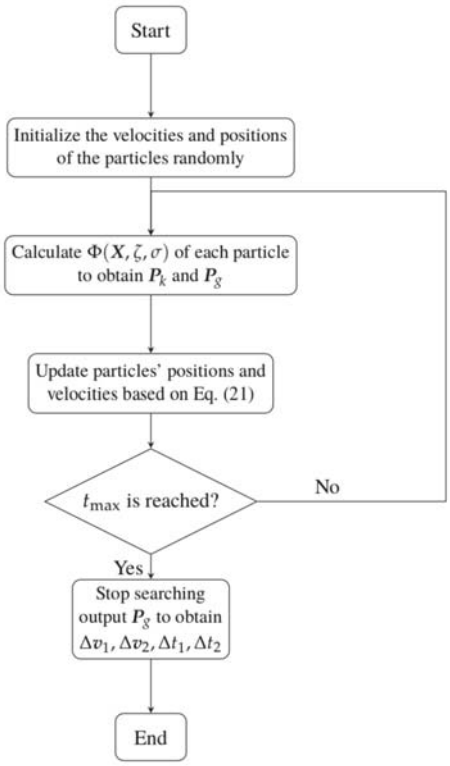

Fig. 3. Flowchart of the IPSO.

1) Design PSO parameters such as N_1, $t_{\max}$, ϖ, c_1, c_2. Express the constraints of $\boldsymbol{X}_k$ and $\boldsymbol{\nu}_k$ in the form of (22). Initialize $\boldsymbol{X}_k$ and $\boldsymbol{\nu}_k$ randomly.

2) Substituting $\boldsymbol{X}_k = \{\Delta v_{k1}, \alpha_{k1}, \beta_{k1}, \Delta E_{k1}, \Delta v_{k2}, \alpha_{k2}, \beta_{k2}, \Delta E_{k2}\}$ into the chaser spacecraft dynamics, and using Eqs. (3) (5) (15) and (17) to calculate the spacecraft velocity changes. Then, calculate $\Phi(\boldsymbol{X}, \zeta, \sigma)$ to obtain $\boldsymbol{P}_k$ and $\boldsymbol{P}_g$.

3) $\boldsymbol{X}_k$ and $\boldsymbol{\nu}_k$ are updated based on Eq. (21). If a particle violates the constraints, set a new $\boldsymbol{X}_k$ and $\boldsymbol{\nu}_k$ for it by Eqs. (27) and (28).

4) Go to Step 2, and update $\boldsymbol{P}_k$ and $\boldsymbol{P}_g$.

5) Repeat Step 3-4 until $t_{\max}$ is reached, and then output $\boldsymbol{P}_g$ to obtain $\Delta\boldsymbol{v}_1, \Delta\boldsymbol{v}_2, \Delta t_1, \Delta t_2$.

4. Attitude controller design and stability analysis

In this section we develop a co-ordinate free, finite-time, attitude controller to guarantee that the thrust direction $\Delta\boldsymbol{v}_i/\parallel\Delta\boldsymbol{v}_i\parallel$ is met as the prescribed time. Firstly, to facilitate the stability analysis of the finite-time attitude controller, two lemmas are presented.

4.1. Lemmas

Lemma 1. *[42] If $\eta_1 > 0$, $\eta_2 > 0$, and $0 < \rho < 1$, then the following inequality holds*

$$(\eta_1 + \eta_2)^\rho \leq \eta_1^\rho + \eta_2^\rho \tag{31}$$

Lemma 2. *[35] Consider a nonlinear system $\dot{\boldsymbol{x}} = g(\boldsymbol{x}), g(0) = 0, \boldsymbol{x} \in \mathbb{R}^n$, where $g(\boldsymbol{x})$ is a continuous function defined on an open neighbourhood $\Im$ of origin, and there exists a continuous positive definite function $V(\boldsymbol{x}) : \mathbb{R}^n \to \mathbb{R}$ defined on $\Im$ such that*

$$\dot{V}(\boldsymbol{x}) \leq -\rho_1 V(\boldsymbol{x}) - \rho_2 V^\rho(\boldsymbol{x}), \forall T > T_0 \tag{32}$$

where $\rho_1 > 0, \rho_2 > 0$, and $0 < \rho < 1$. Then $\boldsymbol{x} = 0$ is a locally finite-time equilibrium point, and the system states can converge to it with the settling time

$$T_f \leq T_0 + \frac{1}{\rho_1(1-\rho)} \ln \frac{\rho_1 V^{1-\rho}(\boldsymbol{x}(t_0)) + \rho_2}{\rho_2} \tag{33}$$

where $\boldsymbol{x}(t_0)$ is the initial value of $\boldsymbol{x}$. Moreover, if $\Im = \mathbb{R}^n$, then $\boldsymbol{x} = 0$ will be a globally stable point.

4.2. Finite-time FTSMC design and stability analysis

The finite-time attitude controller will be designed based on the relative rotational dynamics of the chaser spacecraft governed by Eqs. (7)-(12). A co-ordinate free sliding surface is designed directly on the Special Orthogonal Group SO(3)

$$\boldsymbol{S} = \boldsymbol{e}_{\boldsymbol{\Omega} i} + \vartheta_1 \boldsymbol{e}_{\boldsymbol{R} i} + \vartheta_2 \mathrm{sig}^{\varphi}(\boldsymbol{e}_{\boldsymbol{R} i}) \tag{34}$$

where $\vartheta_1 > 0$, $\vartheta_2 > 0$, $0 < \varphi < 1$, and $\mathrm{sig}^{\varphi}(\boldsymbol{e}_{\boldsymbol{R} i}) = \Big[\big|[\boldsymbol{e}_{\boldsymbol{R} i}]_1\big|^{\varphi} \mathrm{sgn}([\boldsymbol{e}_{\boldsymbol{R} i}]_1), \cdots, \big|[\boldsymbol{e}_{\boldsymbol{R} i}]_3\big|^{\varphi} \mathrm{sgn}([\boldsymbol{e}_{\boldsymbol{R} i}]_3) \Big]^{\mathrm{T}}$. Taking the derivative of $\boldsymbol{S}$, and substituting Eqs. (11) and (12) into it, then the attitude dynamics of the chaser spacecraft can be modified to

$$\dot{\boldsymbol{S}} = \dot{\boldsymbol{e}}_{\boldsymbol{\Omega} i} + \vartheta_1 \dot{\boldsymbol{e}}_{\boldsymbol{R} i} + \vartheta_2 \varphi |\boldsymbol{e}_{\boldsymbol{R} i}|^{\varphi - 1} \dot{\boldsymbol{e}}_{\boldsymbol{R} i} = \boldsymbol{J}^{-1}(-\boldsymbol{\Omega}_i^{\times} \boldsymbol{J} \boldsymbol{\Omega}_i + \boldsymbol{U}_i) + \boldsymbol{L} \tag{35}$$

where $\boldsymbol{L} = \boldsymbol{\Omega}_i^{\times} \boldsymbol{R}_{ei}^{\mathrm{T}} \boldsymbol{\Omega}_{di} - \boldsymbol{R}_{ei}^{\mathrm{T}} \dot{\boldsymbol{\Omega}}_{di} + \vartheta_1 \boldsymbol{G}_i(\boldsymbol{R}_i, \boldsymbol{R}_{di}) \boldsymbol{e}_{\boldsymbol{\Omega} i} + \vartheta_2 \varphi |\boldsymbol{e}_{\boldsymbol{R} i}|^{\varphi - 1} \boldsymbol{G}_i(\boldsymbol{R}_i, \boldsymbol{R}_{di}) \boldsymbol{e}_{\boldsymbol{\Omega} i}$. Next, based on Eqs. (34) and (35), the major result of this section can be summarized as follows:

Theorem 1. *Consider the spacecraft attitude error dynamics governed by Eqs. (34) and (35). Design the attitude control law as*

$$\boldsymbol{U}_i = \boldsymbol{\Omega}_i^{\times} \boldsymbol{J} \boldsymbol{\Omega}_i - \boldsymbol{J} \boldsymbol{L} - \frac{K_1}{K_3} \boldsymbol{S} - \frac{K_2}{K_3} \mathrm{sig}^{\varphi}(\boldsymbol{S}) - \frac{1}{K_3} \boldsymbol{e}_{\boldsymbol{R} i} \tag{36}$$

where K_1, K_2, and K_3 are all positive constants. Then, the finite-time stability of the closed-loop attitude system can be guaranteed, which means $\lim_{T_i \to T_{fi}} \boldsymbol{e}_{\boldsymbol{R} i} = 0$. The estimation of the attraction region is

$$\Theta = \Big\{ (\boldsymbol{R}_i, \boldsymbol{R}_{di}) \in \mathrm{SO}(3) : \Psi_i(\boldsymbol{R}_i, \boldsymbol{R}_{di}) < \Upsilon_{\boldsymbol{R} e} \text{ and } \| \boldsymbol{S} \|^2 < \frac{2}{K_3 \lambda_{\max}(\boldsymbol{J})} \big(\Upsilon_{\boldsymbol{R} e} - \Psi_i(\boldsymbol{R}_i, \boldsymbol{R}_{di}) \big) \Big\} \tag{37}$$

where $\Upsilon_{\boldsymbol{R} e} = \Lambda(\mathrm{tr}(\boldsymbol{K}) \boldsymbol{I}_3 - \boldsymbol{K}) > 0$. Therefore, the z_b axis of the chaser spacecraft can rotate to the direction of $\Delta \boldsymbol{v}_i$ in finite-time.

Proof. To prove the finite-time stability of the resulted closed-loop system, we consider the following candidate Lyapunov function:

$$V = \Psi_i(\boldsymbol{R}_i, \boldsymbol{R}_{di}) + \frac{K_3}{2} \boldsymbol{S}^{\mathrm{T}} \boldsymbol{J} \boldsymbol{S} \tag{38}$$

Taking the derivative of V along Eq.(35), and substituting Eq. (8) into it, one can obtain

$$\begin{aligned} \dot{V} &= \dot{\Psi}_i(\boldsymbol{R}_i, \boldsymbol{R}_{di}) + K_3 \boldsymbol{S}^{\mathrm{T}} \boldsymbol{J} \dot{\boldsymbol{S}} \\ &= \boldsymbol{e}_{\boldsymbol{R} i} \boldsymbol{e}_{\boldsymbol{\Omega} i} + K_3 \boldsymbol{S}^{\mathrm{T}} \boldsymbol{J} \Big(\boldsymbol{J}^{-1}(-\boldsymbol{\Omega}_i^{\times} \boldsymbol{J} \boldsymbol{\Omega}_i + \boldsymbol{U}_i) + \boldsymbol{L} \Big) \end{aligned} \tag{39}$$

Substituting the designed controller Eq. (36) into it, yields

$$\begin{aligned}\dot{V} &= \boldsymbol{e}_{\boldsymbol{R}i}\boldsymbol{e}_{\boldsymbol{\Omega}i} + K_3\boldsymbol{S}^{\mathrm{T}}\big(-\frac{K_1}{K_3}\boldsymbol{S} - \frac{K_2}{K_3}\mathrm{sig}^{\varphi}(\boldsymbol{S}) - \frac{1}{K_3}\boldsymbol{e}_{\boldsymbol{R}i}\big)\\ &= \boldsymbol{e}_{\boldsymbol{R}i}\boldsymbol{e}_{\boldsymbol{\Omega}i} - K_1\boldsymbol{S}^{\mathrm{T}}\boldsymbol{S} - K_2\boldsymbol{S}^{\mathrm{T}}\mathrm{sig}^{\varphi}(\boldsymbol{S}) - \boldsymbol{S}^{\mathrm{T}}\boldsymbol{e}_{\boldsymbol{R}i}\end{aligned} \tag{40}$$

From Eq. (34), it is obvious that

$$\boldsymbol{e}_{\boldsymbol{\Omega}i} = \boldsymbol{S} - \vartheta_1\boldsymbol{e}_{\boldsymbol{R}i} - \vartheta_2\mathrm{sig}^{\varphi}(\boldsymbol{e}_{\boldsymbol{R}i}) \tag{41}$$

Taking Eq. (41) into (40), after some algebraic manipulations, we have

$$\dot{V} \leq -\vartheta_1 \parallel \boldsymbol{e}_{\boldsymbol{R}i} \parallel^2 -\vartheta_2 \parallel \boldsymbol{e}_{\boldsymbol{R}i} \parallel^{1+\varphi} -K_1 \parallel \boldsymbol{S} \parallel^2 -K_2 \parallel \boldsymbol{S} \parallel^{1+\varphi} \tag{42}$$

From the Property 1 of $\Psi_i(\boldsymbol{R}_i, \boldsymbol{R}_{di})$ in (13), we have $\frac{\Psi_i(\boldsymbol{R}_i, \boldsymbol{R}_{di})}{b_2} \leq \parallel \boldsymbol{e}_{\boldsymbol{R}i} \parallel^2$. Then (42) can be changed to

$$\begin{aligned}\dot{V} \leq& -\frac{\vartheta_1}{b_2}\Psi_i(\boldsymbol{R}_i, \boldsymbol{R}_{di}) - \frac{2K_1}{K_3\lambda_{\max}(\boldsymbol{J})}\frac{K_3}{2}\boldsymbol{S}^{\mathrm{T}}\boldsymbol{J}\boldsymbol{S}\\ &- \frac{\vartheta_2}{b_2^{(1+\varphi)/2}}\Psi_i^{(1+\varphi)/2}(\boldsymbol{R}_i, \boldsymbol{R}_{di}) - K_2\Big(\frac{2}{K_3\lambda_{\max}(\boldsymbol{J})}\Big)^{(1+\varphi)/2}\Big(\frac{K_3}{2}\boldsymbol{S}^{\mathrm{T}}\boldsymbol{J}\boldsymbol{S}\Big)^{(1+\varphi)/2}\\ \leq& -K_a\Big(\Psi_i(\boldsymbol{R}_i, \boldsymbol{R}_{di}) + \frac{K_3}{2}\boldsymbol{S}^{\mathrm{T}}\boldsymbol{J}\boldsymbol{S}\Big) - K_b\Big(\Psi_i^{(1+\varphi)/2}(\boldsymbol{R}_i, \boldsymbol{R}_{di}) + (\frac{K_3}{2}\boldsymbol{S}^{\mathrm{T}}\boldsymbol{J}\boldsymbol{S})^{(1+\varphi)/2}\Big)\end{aligned} \tag{43}$$

where $\lambda_{\max}(\cdot)$ is the maximum eigenvalue of a matrix, and

$$\begin{aligned}K_a &= \min\Big\{\frac{\vartheta_1}{b_2}, \frac{2K_1}{K_3\lambda_{\max}(\boldsymbol{J})}\Big\} > 0\\ K_b &= \min\Big\{\frac{\vartheta_2}{b_2^{(1+\varphi)/2}}, K_2\Big(\frac{2}{K_3\lambda_{\max}(\boldsymbol{J})}\Big)^{(1+\varphi)/2}\Big\} > 0\end{aligned} \tag{44}$$

Since $\Psi_i(\boldsymbol{R}_i, \boldsymbol{R}_{di}) > 0$, $\frac{K_3}{2}\boldsymbol{S}^{\mathrm{T}}\boldsymbol{J}\boldsymbol{S} > 0$, and $0 < \frac{1+\varphi}{2} < 1$, thus by using Lemma 1, the following inequality can be obtained

$$\Big(\Psi_i^{(1+\varphi)/2}(\boldsymbol{R}_i, \boldsymbol{R}_{di}) + (\frac{K_3}{2}\boldsymbol{S}^{\mathrm{T}}\boldsymbol{J}\boldsymbol{S})^{(1+\varphi)/2}\Big) \geq \Big(\Psi_i(\boldsymbol{R}_i, \boldsymbol{R}_{di}) + \frac{K_3}{2}\boldsymbol{S}^{\mathrm{T}}\boldsymbol{J}\boldsymbol{S}\Big)^{(1+\varphi)/2} \tag{45}$$

Then, substituting (45) into (43) yields

$$\begin{aligned}\dot{V} &\leq -K_a\Big(\Psi_i(\boldsymbol{R}_i, \boldsymbol{R}_{di}) + \frac{K_3}{2}\boldsymbol{S}^{\mathrm{T}}\boldsymbol{J}\boldsymbol{S}\Big) - K_b\Big(\Psi_i(\boldsymbol{R}_i, \boldsymbol{R}_{di}) + \frac{K_3}{2}\boldsymbol{S}^{\mathrm{T}}\boldsymbol{J}\boldsymbol{S}\Big)^{(1+\varphi)/2}\\ &\leq -K_aV - K_bV^{(1+\varphi)/2}\end{aligned} \tag{46}$$

Then from Lemma 2, we can find that $\Psi_i(\boldsymbol{R}_i, \boldsymbol{R}_{di})$ and $\boldsymbol{S}$ can reach 0 in finite-time. From Property 1 of $\Psi(\boldsymbol{R}, \boldsymbol{R}_d)$, we know that $\boldsymbol{R}_i = \boldsymbol{R}_{di}$ is the unique solution of $\Psi_i(\boldsymbol{R}_i, \boldsymbol{R}_{di}) = 0$. When $\boldsymbol{R}_i = \boldsymbol{R}_{di}$, we can get $\boldsymbol{e}_{\boldsymbol{R}i} = 0$ from Eq. (9). Substituting $\boldsymbol{e}_{\boldsymbol{R}i} = 0$ and $\boldsymbol{S} = 0$ into Eq. (41) yields $\boldsymbol{e}_{\boldsymbol{\Omega}i} = 0$. □

Note that in this paper the disturbances are assumed to be negligible in the first two phases of a RPO. However, in the presence of significant disturbances the control can be adapted to include a disturbance rejection component with the inclusion of an extended state observer. In addition, an alternative approach would be to include moving mass control technology [43–45] which can counteract the disturbance torques to maintain stabilization by momentum exchange using internal moving masses.

The overall control strategy can be summarized as follows: 1) Using the PSO to obtain the optimal two impulse vectors and their running times, namely $[\Delta\boldsymbol{v}_1]_o$, $[\Delta\boldsymbol{v}_2]_o$, Δt_1, and Δt_2. 2) Applying the attitude controller (36) to control the z_b axis of the chaser spacecraft to the directions of $[\Delta\boldsymbol{v}_1]_o$ and $[\Delta\boldsymbol{v}_2]_o$, respectively. Then, the actual velocity changes $[\Delta\boldsymbol{v}_1]_a, [\Delta\boldsymbol{v}_2]_a$ can be obtained. The subscripts $[\cdot]_o$ and $[\cdot]_a$ are used to represent the parameters of optimal and actual trajectory, respectively. 3) Using Eq. (3) to calculate the actual position and velocity of the chaser spacecraft at $t_3 = t_1 + \Delta t_1 + \Delta t_2$. 4) Using Lambert method to get the last two impulse vectors. 5) Repeating step 2 and 3 to obtain the actual positions and velocities of the chaser spacecraft at t_3 and t_f. Then, the chaser spacecraft can track the trajectory of the target spacecraft in finite time.

5. Simulation results

5.1. Simulation setup

In this section, several numerical examples are conducted to verify the effectiveness of the improved PSO for optimal spacecraft rendezvous motion planning and the attitude control scheme for thrust-vectoring spacecraft trajectory tracking. We set the preparation time for the chaser spacecraft to calculate its optimal trajectory and rotate its attitude to the direction of $\Delta\boldsymbol{v}_i$ to be $\Delta t_i^{rotate} = 200s$, and the attitude of the chaser spacecraft when it is free of control is assumed that $\mathscr{F}_b$ is perfectly aligned with its orbit frame $\mathscr{F}_o$, and from the rotation matrix of $\mathscr{F}_I$ to $\mathscr{F}_o$ in [31] we can get $[\boldsymbol{R}_i]^{\mathrm{T}}_{initial} = \boldsymbol{R}_z(w_i + [\theta_{ci}]_{initial})\boldsymbol{R}_x(I_i)\boldsymbol{R}_z(W_i)$, where $[\theta_{ci}]_{initial}$ is the true anomaly when the attitude controller starts to act on the spacecraft, and $\boldsymbol{R}_x(\cdot)$ and $\boldsymbol{R}_z(\cdot)$ stand for transformation matrices about x_{axis} and z_{axis} by angles $w_i + [\theta_{ci}]_{initial}$, I_i, and W_i, respectively. The orbit transfer time is $t_f = 10000s$. The orbital elements of the target spacecraft and the chaser spacecraft at $t_1 = 0$ are given in Table. 1. The position of the target spacecraft at $t_f = 10000s$ can be calculated using its orbit elements based on Eqs. (3)-(5). The system parameters of the chaser spacecraft are assumed to be $\boldsymbol{J} = \mathrm{diag}(400, 400, 400)\mathrm{kg}\cdot\mathrm{m}^2$ and $m = 400\mathrm{kg}$, the search space of velocity is defined by $0 \le \Delta v_i \le 2$ km/s, $i = 1,\ 2$, and the upper bound of the control torque is $u_{\max} = 4\mathrm{N}\cdot\mathrm{m}$.

Table 1: Orbit elements of the target spacecraft and the chaser spacecraft at t_1.

Orbit parameters	The target spacecraft	The chaser spacecraft
Semi-major axis	27500km	7800km
Eccentricity	0.12	0.2
Inclination	50°	45°
Argument of perigee	80°	55°
Mean anomaly	0	-5°
Right ascension of ascending node (RAAN)	60°	30°

For the purpose of comparison, two cases are considered in the simulations. Case A: comparison between the optimal velocity deviations generated by conventional PSO (CPSO is the short of it) and the improved PSO in this paper to show the priority of the IPSO, and Case B: final position and velocity comparisons between ideal trajectory and actual trajectory where the directions of $\Delta \boldsymbol{v}_i$ are controlled by the attitude controller (36), to show the performance of the proposed control strategy.

5.2. Comparison between CPSO and IPSO

The population size of the swarm is $N_1 = 40$ and $t_{\max} = 1000$, which will be fixed for these two scenarios. For the IPSO, the parameters are designed as follows: $\sigma = 100$, $\gamma_1 = 2.5$, $\gamma_2 = 0.5$, $\Theta_1 = 1.8$, $\Theta_2 = 1.6$, $\varpi_0 = 0.9$, $\varpi_f = 0.4$, and $\zeta_1 = 1$. In the CPSO, the linear weight of ϖ is still used, but the constraint-handling mechanism is not considered, and the two learning factors c_1 and c_2 are equal to 2.

Table 2: Variables optimized by IPSO.

Impulse i	$\Delta \boldsymbol{v}_i$ (km/s)	$\alpha_i/(^\circ)$	$\beta_i/(^\circ)$	t_i(s)
1	1.9402	64.326	103.09	0
2	0.8366	54.563	115.67	0
3	1.811	55.36	336.213	1893.9
4	1.8447	-59.372	286.33	10000

Table 3: Variables optimized by CPSO.

Impulse i	$\Delta \boldsymbol{v}_i$ (km/s)	$\alpha_i/(^\circ)$	$\beta_i/(^\circ)$	t_i(s)
1	2	52.57	133.3	0
2	0	-	-	1453.3
3	2.60	79.0	1.46	1453.3
4	2.081	-58.1	285.04	10000

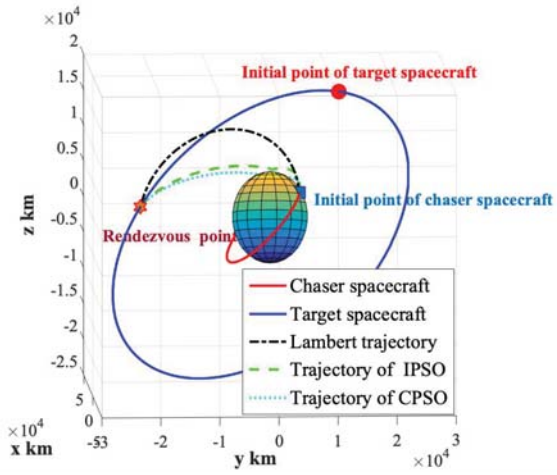

Fig. 4. Rendezvous trajectory generated by IPSO and CPSO

Several independent simulations are undertaken for each PSO version to obtain the optimal solutions. The trajectories generated by IPSO, CPSO and Lambert method are shown in Fig. 4, from which we can see that the boundary conditions are well satisfied in each scenario. Since the final position and the running time are naturally satisfied in both of the optimization methods, what we care about is the total velocity deviations. The variables optimized by IPSO are shown in Table. 2, and the counterparts of CPSO are given in Table. 3, from which we can find that all the optimal solutions satisfy the constraints in (19). From the results, we can conclude that three impulses are enough to track the trajectory of the target spacecraft, since the first and second impulses of IPSO can be finished at the initial time, and the second impulse of CPSO is zero. Moreover, to illustrate that compared with the Lambert method, both the solutions of IPSO and CPSO are optimal, the values of the cost functions of these three methods are calculated

$$\begin{aligned} J_{\text{Lambert}} &= \sum_{i=1}^{4} \Delta v_i = 8.6504\text{km/s} \\ J_{\text{CPSO}} &= \sum_{i=1}^{4} \Delta v_i = 6.6825\text{km/s} \\ J_{\text{IPSO}} &= \sum_{i=1}^{4} \Delta v_i = 6.4326\text{km/s} \end{aligned} \tag{47}$$

from which we can conclude that the performance of IPSO is the best.

5.3. Performance of the finite-time attitude controller

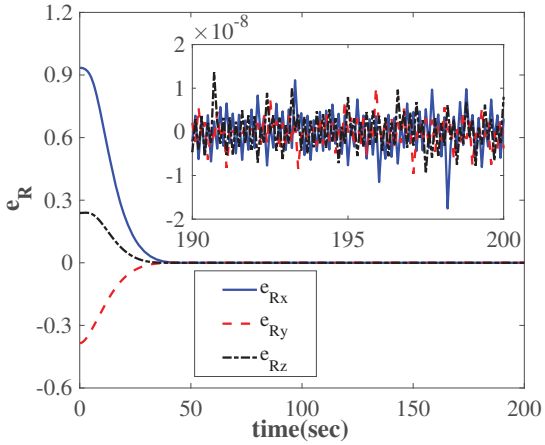

Fig. 5. Time responses of $\boldsymbol{e}_{\boldsymbol{R}1}$.

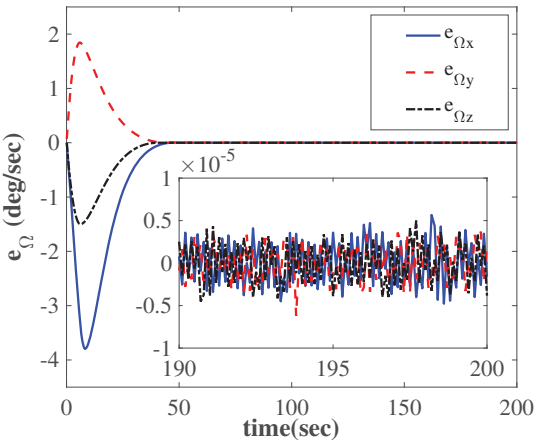

Fig. 6. Time responses of $\boldsymbol{e}_{\boldsymbol{\Omega}1}$.

Table 4: Attitude tracking errors during each impulse

Time	Attitude tracking errors
$t = 0$	$\boldsymbol{e}_{\boldsymbol{R}_{12}} = [-0.206377015352078; 0.606097465124340; 0.443675718436785] \times 10^{-8}$
$i = 1, 2$	$\boldsymbol{e}_{\boldsymbol{\Omega}_{12}} = [0.068507994451558; -0.235551161964597; -0.296230314701513] \times 10^{-5}$(deg/sec)
$t = 1893.9$s	$\boldsymbol{e}_{\boldsymbol{R}_3} = [0.399986779656952; 0.334045627691576; -0.420339094267647] \times 10^{-8}$
$i = 3$	$\boldsymbol{e}_{\boldsymbol{\Omega}_3} = [-0.257768903573084; -0.339839817984818; 0.224325970036670] \times 10^{-5}$(deg/sec)
$t = 10000$s	$\boldsymbol{e}_{\boldsymbol{R}_4} = [-0.402183533587733; 0.477246542571585; 0.285693660800068] \times 10^{-8}$
$i = 4$	$\boldsymbol{e}_{\boldsymbol{\Omega}_4} = [0.234936401269850; -0.295155587973101; -0.426356100674213] \times 10^{-5}$(deg/sec)

The optimal solutions of IPSO are applied, and the requirement for the attitude controller is to control the z_b axis of the chaser spacecraft to the directions of $\Delta \boldsymbol{v}_i$ in finite-time, while $\| \boldsymbol{U}_i \| \leq u_{\max}$. The guideline of choosing the parameters of the attitude controller is by trial-and-error until a good control performance is obtained, and the parameters are designed to be: $\boldsymbol{K} = \mathrm{diag}(0.8, 1.25, 1)$, $\vartheta_1 = 0.03$, $\vartheta_2 = 0.05$, $\varphi = 2/3$, $K_1 = 12$, $K_2 = 15$ and $K_3 = 0.5$. The attitude tracking errors over the entire mission are given in Table. 4 to illustrate the performance of the attitude controller. Moreover, for the sake of brevity, only the plots of the first two impulses are provided, and the simulation results under the attitude controller (36) are presented

in Figs. 5-7. Figs. 5 and 6 show the time responses of the attitude tracking errors in term of $\boldsymbol{e_R}$, and $\boldsymbol{e_{Ri}} = 0$ means the direction of $\Delta \boldsymbol{v}_i$ has been synchronized by the z_b axis of the chaser spacecraft under the effect of the attitude controller. From the plots it can be seen that the attitude motion falls to tolerance with the settling time about 50s. Thus, the preparation time $\Delta t_i^{rotate} = 200s$ is enough for the chaser spacecraft to prepare for the rendezvous process. In addition, the plots of the corresponding control torques applied on the chaser spacecraft during the operation of the first two impulses are shown in Fig. 7, from which we can see that the control limit in (18) is satisfied.

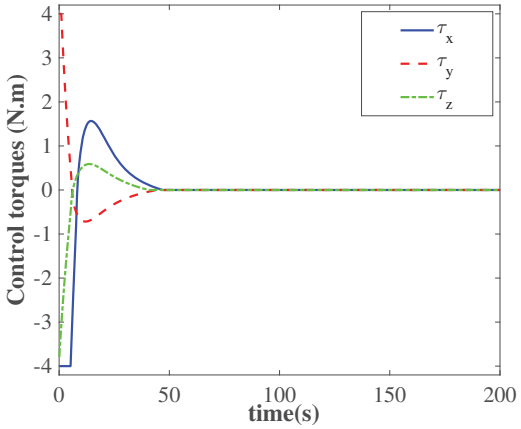

Fig. 7. Time responses of control torques.

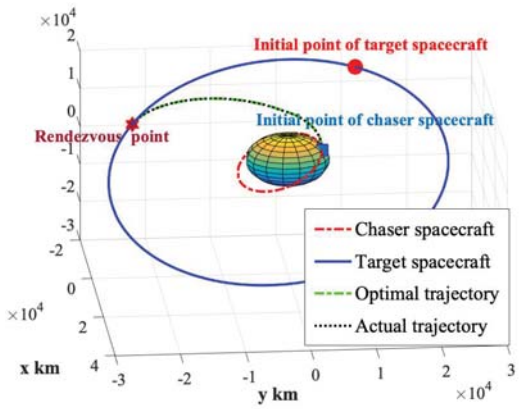

Fig. 8. Ideal rendezvous trajectory and the actual trajectory under controller (36).

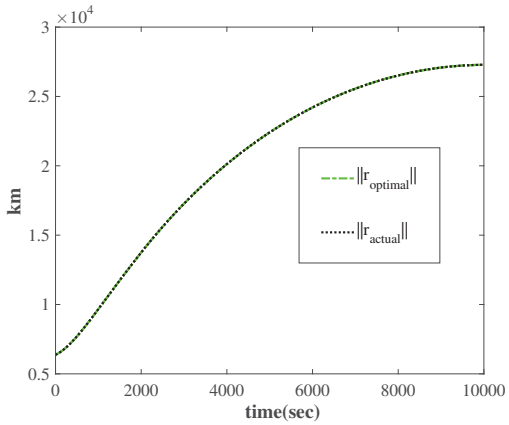

Fig. 9. Norms of the positions of the two cases.

Moreover, to show the proposed attitude controller can guarantee that thrust-vectoring spacecraft rendezvous maneuver can be undertaken with high accuracy, comparisons between the positions and velocities of the ideal trajectory and the actual trajectory are conducted. The plots of the ideal trajectory optimized by the IPSO and the actual trajectory, where the thruster directions are controlled by the attitude controller, are shown in Fig. 8, and the plots of the norms of $\boldsymbol{r}_{\text{optimal}}$ and $\boldsymbol{r}_{\text{actual}}$ are shown in Fig. 9. From these two

figures, it can be seen that with the proposed attitude control scheme, the optimal rendezvous trajectory can be tracked by the actual trajectory. To this end, the specific positions and velocities of the ideal trajectory and the actual trajectory before and after each impulse are given in Table. 5 to illustrate the performance of the proposed algorithm. As illustrated in the table, during the trajectory tracking maneuver, the tracking errors are at most 0.42m and 3.2×10^{-4}m/s. From these simulation results we can conclude that the trajectory of the target spacecraft can be tracked in a specified time with high-precision performance.

Table 5: Actual and ideal positions and velocities of the chaser spacecraft during each impulse

	Position and velocity values during each impulse	Tracking errors
	$[\boldsymbol{r}_{12}^-]_o = [\boldsymbol{r}_{12}^+]_o = [2083.498682; 5033.403198; 3317.305696]$km	$\parallel [\Delta \boldsymbol{r}_{12}]_{oa} \parallel = 0$
	$[\boldsymbol{v}_{12}^-]_o = [-7.742920794; -0.164226658; 3.729235939]$km/s	
$t = 0$	$[\boldsymbol{v}_{12}^+]_o = [-8.016187926; 1.007304367; 6.231925781]$km/s	$\parallel [\Delta \boldsymbol{v}_{12}]_{oa}^- \parallel = 0$
$i = 1, 2$	$[\boldsymbol{r}_{12}^-]_a = [\boldsymbol{r}_{12}^+]_a = [2083.498682; 5033.403198; 3317.305696]$km	
	$[\boldsymbol{v}_{12}^-]_a = [-7.742920794; -0.164226658; 3.729235939]$km/s	$\parallel [\Delta \boldsymbol{v}_{12}]_{oa}^+ \parallel = 1.37 \times 10^{-4}$m/s
	$[\boldsymbol{v}_{12}^+]_a = [-8.016187881; 1.007304324; 6.231925659]$km/s	
	$[\boldsymbol{r}_3^-]_o = [\boldsymbol{r}_3^+]_o = [-11111.824828; 32.000436; 7366.509275]$km	$\parallel [\Delta \boldsymbol{r}_3]_{oa} \parallel = 0.42$m
	$[\boldsymbol{v}_3^-]_o = [-4.934498155; -3.805812081; -0.290350922]$km/s	
$t = 1893.9$s	$[\boldsymbol{v}_3^+]_o = [-3.992479666; -4.221012678; 1.199677979]$km/s	$\parallel [\Delta \boldsymbol{v}_3]_{oa}^- \parallel = 3.2 \times 10^{-4}$m/s
$i = 3$	$[\boldsymbol{r}_3^-]_a = [\boldsymbol{r}_3^+]_a = [-11111.824659; 32.000264; 7366.508937]$km	
	$[\boldsymbol{v}_3^-]_a = [-4.934497973; -3.805812187; -0.290351162]$km/s	$\parallel [\Delta \boldsymbol{v}_3]_{oa}^+ \parallel = 1.2 \times 10^{-4}$m/s
	$[\boldsymbol{v}_3^+]_a = [-3.992479772; -4.22101273; 1.199678007]$km/s	
	$[\boldsymbol{r}_f^-]_o = [\boldsymbol{r}_f^+]_o = [-15369.00349; -22398.14162; 2515.64482]$km	$\parallel [\Delta \boldsymbol{r}_f]_{oa} \parallel = 0.17$m
	$[\boldsymbol{v}_f^-]_o = [1.353060878; -1.088220548; -1.267736554]$km/s	
$t = 10000$s	$[\boldsymbol{v}_f^+]_o = [1.617343450; -1.990128898; -2.855113831]$km/s	$\parallel [\Delta \boldsymbol{v}_f]_{oa}^- \parallel = 2.7 \times 10^{-5}$m/s
$i = 4$	$[\boldsymbol{r}_f^-]_a = [\boldsymbol{r}_f^+]_a = [-15369.00361; -22398.14174; 2515.64482]$km	
	$[\boldsymbol{v}_f^-]_a = [1.353075924; -1.088198549; -1.267738963]$km/s	$\parallel [\Delta \boldsymbol{v}_f]_{oa}^+ \parallel = 1 \times 10^{-4}$m/s
	$[\boldsymbol{v}_f^+]_a = [1.617343431; -1.990128861; -2.855113738]$km/s	

6. Conclusions

A constrained optimal orbit-attitude trajectory generation method is proposed for thrust-vectoring spacecraft rendezvous missions. In particular, the chaser spacecraft is equipped with a single impulsive thruster that is pointed using a precise, finite-time, attitude control. It is shown that a typical rendezvous can be undertaken with a thrust-vectored spacecraft using only 4 impulsive maneuvers. This scheme uses an improved particle swarm optimization (PSO) to obtain the desired thruster pulse durations and desired attitude matrix. A coordinate-free finite-time attitude controller is designed, which enables the four impulses to be delivered accurately and precisely at the required time. Formulating the problem on SO(3) allows the reference attitude to be defined in a natural way, with one of the orthonormal vectors of the reference attitude aligned with the thrust direction. The proposed finite-time attitude control formulation also has the advantage that it does not require the computation of higher-order derivatives of the error function, which is usually required to guarantee finite-time stability. From the simulation results, we can conclude that: 1) The optimal trajectory obtained by the improved PSO requires less $\Delta \boldsymbol{v}$ than a conventional PSO; 2) The attitude controller is able to track the desired force vectors with a settling time no more than 50s, while satisfying the torque constraints on the reaction wheels; 3) The real-time implementation of the proposed control scheme can track the optimal trajectory generated by the improved PSO with a position error less than 0.2m, which is within the requirements of the spacecraft rendezvous missions described in [4].

Conflict of interest statement

The authors declare that they have no conflict of interest to this work.

Acknowledgements

This work is supported by the China Scholarship Council.

References

[1] M. Pontani, P. Ghosh, B. A. Conway, Particle swarm optimization of multiple-burn rendezvous trajectories, Journal of Guidance, Control, and Dynamics 35 (4) (2012) 1192–1207. doi:10.2514/1.55592.

[2] Q. Li, J. Yuan, B. Zhang, H. Wang, Disturbance observer based control for spacecraft proximity operations with path constraint, Aerospace Science and Technology 79 (2018) 154–163. doi:10.1016/j.ast.2018.05.042.

[3] D. Zhou, Y. Zhang, S. Li, Receding horizon guidance and control using sequential convex programming for spacecraft 6-dof close proximity, Aerospace Science and Technology 87 (2019) 459–477. doi:10.1016/j.ast.2019.02.041.

[4] Y. Chen, Z. He, D. Zhou, Z. Yu, S. Li, Integrated guidance and control for microsatellite real-time automated proximity operations, Acta Astronautica 148 (2018) 175–185. doi:10.1016/j.actaastro.2018.04.054.

[5] L. Sun, W. Huo, Robust adaptive relative position tracking and attitude synchronization for spacecraft rendezvous, Aerospace Science and Technology 41 (2015) 28–35. doi:10.1016/j.ast.2014.11.013.

[6] Y. Wang, H. Ji, Integrated relative position and attitude control for spacecraft rendezvous with iss and finite-time convergence, Aerospace Science and Technology 85 (2019) 234–245. doi:10.1016/j.ast.2018.12.005.

[7] Q. Hu, W. Chen, L. Guo, Fixed-time maneuver control of spacecraft autonomous rendezvous with a free-tumbling target, IEEE Transactions on Aerospace and Electronic Systems 55 (2) (2019) 562–577. doi:10.1109/TAES.2018.2852439.

[8] A. Shirazi, J. Ceberio, J. A. Lozano, Spacecraft trajectory optimization: A review of models, objectives, approaches and solutions, Progress in Aerospace Sciences 102 (2018) 76–98. doi:10.1016/j.paerosci.2018.07.007.

[9] J. A. Starek, B. Açıkmeşe, I. A. Nesnas, M. Pavone, Spacecraft autonomy challenges for next-generation space missions, Springer, 2016, pp. 1–48. doi:10.1007/978-3-662-47694-9.

[10] D. Invernizzi, M. Lovera, L. Zaccarian, Dynamic attitude planning for trajectory tracking in thrust-vectoring uavs, IEEE Transactions on Automatic Control, (2019) to be published.doi:10.1109/TAC.2019.2919660.

[11] R. Haghighi, C. K. Pang, Robust concurrent attitude-position control of a swarm of underactuated nanosatellites, IEEE Transactions on Control Systems Technology 26 (1) (2017) 77–88. doi:10.1109/TCST.2017.2656025.

[12] H. C. Henninger, J. D. Biggs, Optimal under-actuated kinematic motion planning on the ϵ-group, Automatica 90 (2018) 185–195. doi:10.1016/j.automatica.2017.12.049.

[13] J. T. Betts, Practical methods for optimal control and estimation using nonlinear programming, Vol. 19, Siam, 2010.

[14] Y. Jia, X. Yang, Optimization of control parameters based on genetic algorithms for spacecraft attitude tracking with input constraints, Neurocomputing 177 (2016) 334–341. doi:10.1016/j.neucom.2015.11.022.

[15] S. Li, X. Huang, B. Yang, Review of optimization methodologies in global and china trajectory optimization competitions, Progress in Aerospace Sciences 102 (2018) 60–75. doi:10.1016/j.paerosci.2018.07.004.

[16] M. Pontani, B. A. Conway, Particle swarm optimization applied to space trajectories, Journal of Guidance, Control, and Dynamics 33 (5) (2010) 1429–1441. doi:10.2514/1.48475.

[17] A. Rahimi, K. Dev Kumar, H. Alighanbari, Particle swarm optimization applied to spacecraft reentry trajectory, Journal of Guidance, Control, and Dynamics 36 (1) (2013) 307–310. doi:10.2514/1.56387.

[18] H. Zhou, X. Wang, Y. Bai, N. Cui, Ascent phase trajectory optimization for vehicle with multi-combined cycle engine based on improved particle swarm optimization, Acta Astronautica 140 (2017) 156–165. doi:10.1016/j.actaastro.2017.08.024.

[19] J. Shan, Y. Ren, Low-thrust trajectory design with constrained particle swarm optimization, Aerospace Science and Technology 36 (2014) 114–124. doi:10.1016/j.ast.2014.04.004.

[20] J. D. Biggs, L. Colley, Geometric attitude motion planning for spacecraft with pointing and actuator constraints, Journal of Guidance, Control, and Dynamics 39 (7) (2016) 1672–1677. doi:10.2514/1.G001514.

[21] B. Xiao, S. Yin, O. Kaynak, Tracking control of robotic manipulators with uncertain kinematics and dynamics, IEEE Transactions on Industrial Electronics 63 (10) (2016) 6439–6449. doi:10.1109/TIE.2016.2569068.

[22] B. Xiao, S. Yin, H. Gao, Reconfigurable tolerant control of uncertain mechanical systems with actuator faults: A sliding mode observer-based approach, IEEE Transactions on Control Systems Technology 26 (4) (2017) 1249–1258. doi:10.1109/TCST.2017.2707333.

[23] H. Gui, G. Vukovich, Distributed almost global finite-time attitude consensus of multiple spacecraft without velocity measurements, Aerospace Science and Technology 75 (2018) 284–296. doi:10.1016/j.ast.2017.12.015.

[24] B. Xiao, Q. Hu, Y. Zhang, Finite-time attitude tracking of spacecraft with fault-tolerant capability, IEEE Transactions on Control Systems Technology 23 (4) (2015) 1338–1350. doi:10.1109/TCST.2014.2364124.

[25] C. Zhang, J. Wang, D. Zhang, X. Shao, Fault-tolerant adaptive finite-time attitude synchronization and tracking control for multi-spacecraft formation, Aerospace Science and Technology 73 (2018) 197–209. doi:10.1016/j.ast.2017.12.004.

[26] J. Bohn, A. K. Sanyal, Almost global finite-time stabilization of rigid body attitude dynamics using rotation matrices, International Journal of Robust and Nonlinear Control 26 (9) (2016) 2008–2022. doi:10.1002/rnc.3399.

[27] S. P. Viswanathan, A. K. Sanyal, E. Samiei, Integrated guidance and feedback control of underactuated robotics system in se(3), Journal of Intelligent and Robotic Systems 89 (1-2) (2018) 251–263. doi:10.1007/s10846-017-0547-0.

[28] T. Lee, Exponential stability of an attitude tracking control system on so(3) for large-angle rotational maneuvers, Systems

and Control Letters 61 (1) (2012) 231–237. doi:10.1016/j.sysconle.2011.10.017.

[29] X. Shi, D. Zhou, Z. Zhou, R. Li, Continuous adaptive-gain finite-time control for rigid body attitude dynamics on so(3), International Journal of Systems Science 50 (1) (2019) 178–190. doi:10.1080/00207721.2018.1551970.

[30] Y. Guo, J. Guo, S. Song, Backstepping control for attitude tracking of the spacecraft under input saturation, Acta Astronautica 138 (2017) 318–325. doi:10.1016/j.actaastro.2017.06.002.

[31] M. J. Sidi, Spacecraft Dynamics and Control: A Practical Engineering Approach, Vol. 7, Cambridge university press, 1997. doi:10.1017/CBO9780511815652.

[32] C. G. Mayhew, A. R. Teel, Synergistic hybrid feedback for global rigid-body attitude tracking on so(3), IEEE Transactions on Automatic Control 58 (11) (2013) 2730–2742. doi:10.1109/TAC.2013.2266852.

[33] T. Lee, Robust adaptive attitude tracking on so(3) with an application to a quadrotor uav, IEEE Transactions on Control Systems Technology 21 (5) (2012) 1924–1930. doi:10.1109/TCST.2012.2209887.

[34] G. Zhang, D. Zhou, D. Mortari, M. R. Akella, Covariance analysis of lambert's problem via lagrange's transfer-time formulation, Aerospace Science and Technology 77 (2018) 765–773. doi:10.1016/j.ast.2018.03.039.

[35] J. Zhang, D. Ye, J. D. Biggs, Z. Sun, Finite-time relative orbit-attitude tracking control for multi-spacecraft with collision avoidance and changing network topologies, Advances in Space Research 63 (3) (2019) 1161–1175. doi:10.1016/j.asr.2018.10.037.

[36] J. Prussing, Optimal four-impulse fixed-time rendezvous in the vicinity of a circular orbit., AIAA Journal 7 (5) (1969) 928–935. doi:10.2514/3.5246.

[37] R. Eberhart, J. Kennedy, Particle swarm optimization, in: Proceedings of the IEEE international conference on neural networks, Vol. 4, Citeseer, IEEE, Perth, WA, Australia, 1995, pp. 1942–1948. doi:10.1109/ICNN.1995.488968.

[38] H. Zhou, X. Wang, B. Bai, N. Cui, Reentry guidance with constrained impact for hypersonic weapon by novel particle swarm optimization, Aerospace Science and Technology 78 (2018) 205–213. doi:10.1016/j.ast.2018.04.024.

[39] Y. Shi, R. C. Eberhart, Empirical study of particle swarm optimization, in: Proceedings of the 1999 Congress on Evolutionary Computation-CEC99 (Cat. No. 99TH8406), Vol. 3, IEEE, 1999, pp. 1945–1950. doi:10.1109/CEC.1999.785511.

[40] R. T. Rockafellar, The multiplier method of hestenes and powell applied to convex programming, Journal of Optimization Theory and applications 12 (6) (1973) 555–562. doi:10.1007/bf00934777.

[41] Z. Hu, D. Zou, Z. Kong, X. Shen, A particle swarm optimization algorithm with time varying parameters, in: 2018 Chinese Control And Decision Conference (CCDC), IEEE, 2018, pp. 4555–4561. doi:10.1109/CCDC.2018.8407919.

[42] S. Yu, X. Yu, B. Shirinzadeh, Z. Man, Continuous finite-time control for robotic manipulators with terminal sliding mode, Automatica 41 (11) (2005) 1957–1964. doi:10.1016/j.automatica.2005.07.001.

[43] J. Li, S. Chen, C. Li, C. Gao, W. Jing, Adaptive control of underactuated flight vehicles with moving mass, Aerospace Science and Technology 85 (2019) 75–84. doi:10.1016/j.ast.2018.12.003.

[44] J. Li, C. Gao, C. Li, W. Jing, A survey on moving mass control technology, Aerospace Science and Technology 82-83 (2018) 594–606. doi:10.1016/j.ast.2018.09.033.

[45] J. Li, C. Gao, W. Jing, Y. Fan, Nonlinear vibration analysis of a novel moving mass flight vehicle, Nonlinear Dynamics 90 (1) (2017) 733–748. doi:10.1007/s11071-017-3691-y.